



**THE TRUSS-LIKE DISCRETE ELEMENT METHOD IN FRACTURE  
AND DAMAGE MECHANICS**

Journal:	<i>Engineering Computations</i>
Manuscript ID:	EC-Feb-2010-0021.R1
Manuscript Type:	Research Article
Keywords:	truss-like discrete element method, damage mechanics, fracture mechanics, stress intensity factors

SCHOLARONE™  
Manuscripts

Review

THE TRUSS-LIKE DISCRETE ELEMENT METHOD IN FRACTURE  
AND DAMAGE MECHANICS

**Abstract**

**Purpose** – It is the purpose of this paper to further develop the truss-like discrete element method (DEM) in order to make it suitable to deal with damage and fracture problems.

**Design/methodology/approach** – Finite and boundary elements are the best developed methods in the field of numerical fracture and damage mechanics. However, these methods are based on a continuum approach, and thus, the modelling of crack nucleation and propagation could be sometimes a cumbersome task. Besides, discrete methods possess the natural ability to introduce discontinuities in a very direct and intuitive way by simply breaking the link between their discrete components. Within this context, the present work extends the capabilities of a truss-like DEM via the introduction of three novel features: a tri-linear elasto-plastic constitutive law; a methodology for crack discretization and the computation of stress intensity factors; and a methodology for the computation of the stress field components from the uniaxial discrete-element results.

**Findings** – Obtained results show the suitability and the performance of the proposed methodologies to solve static and dynamic crack problems (including crack propagation) in brittle and elasto-plastic materials. Computed results are in good agreement with experimental and numerical results reported in the bibliography.

**Originality/value** – The scope of the truss-like DEM has been extended. New procedures have been introduced to deal with elastoplastic crack problems and to improve the post processing of the stress results.

**Research implications** – This paper demonstrates the versatility of the truss-like DEM to deal with damage mechanics problems. The approach used in this work can be extended to the implementation of time dependent damage mechanisms. Besides, the capabilities of the discrete approach could be exploited by coupling the truss-like DEM to finite and boundary element methods. Coupling strategies would allow using the DEM to model the regions of the problem where crack nucleation and propagation occurs, while finite or boundary elements are used to model the undamaged regions.

**Keywords:** truss-like discrete element method; damage mechanics; fracture mechanics; stress intensity factors.

**Paper type:** Research paper

## Introduction

During the 1960s an alternative set of computational methods that do not use a set of differential or integral equations to describe the problem were introduced. Depending on the individual element introduced, such as particles, agents or molecules, methods such as molecular dynamics (MD), discrete element (DEM), discontinuous deformation analysis (DDA), and similar were invented. In the process, computational mechanics of discontinua emerged, and its is now an integral part of cutting edge research in nanotechnology and industrial processes spanning over diverse fields as mining, milling, pharmaceuticals, powders, ceramics, composites, blasting, construction, etc (Munjiza, 2009).

The numerical simulation of fracture and damage problems is always an active research topic. Finite and boundary element methods are the best developed methods in this field (see for instance Anderson, 2005 and Aliabadi and Rooke, 1991). However, these methods are based on a continuum approach, and thus the modelling of crack nucleation and propagation could be a cumbersome task. In contrast, it could be argued that discrete methods have the natural ability to introduce discontinuities in a very direct and intuitive way by simply breaking the link between their discrete components. Moreover, discrete methods offer a convenient framework to account for the disorder of the material microstructure by means of statistical models. This feature constitutes an advantage over traditional continuum models of micromechanics which adopt homogenization techniques to convert a disordered material into an equivalent continuum model. This approach, reasonable in the pristine state, is not realistic in presence of cooperative phenomena between existing defects and/or microcracks (Rinaldi et al, 2008). Within this context, it is explored in this paper the application of a truss-like DEM to deal with fracture and damage problems.

The utilization of discrete elements to represent a solid continuum can be tracked back to the pioneering work by Hrenikoff (1941) who used arrays of solid bars with this purpose. Absi (1971) developed a similar idea, and used bar arrays to simulate elastic foundations

and structural walls in tall buildings. Another important early work was that by Cundall and Strack (1979), who represented the continuum using discrete elements to simulate the behaviour of granular soils in geotechnical problems.

More recently, a number of discrete element methods for solid mechanics have been proposed. These methods are mainly two-dimensional, and they use either beam or truss lattices. Among others, beam lattices were used by Schlangen and Garboczi (1997) and Chiaia et al (1997) to study different aspects of the quasi-fragile fracture of cementitious materials. Discrete formulations based on truss lattices were introduced by Fraternali et al (2002) to solve small deformations of generally anisotropic plane continua; by Slepian (2005) to model crack propagation and by Rinaldi and Lai (2007) and Rinaldi et al (2008) to estimate the damage and effective mechanical properties of disordered microstructures. Moreover, DEMs were coupled to the finite element method (FEM) to deal with damage mechanics problems. Among others, Klerck et al (2004) developed an explicit FEM-DEM formulation to model discrete fracture in quasi-brittle geomaterials, while Cottrel et al (2003) introduced a finite-element discrete-particle method to model the erosion of ceramic materials when subjected to large-scale dynamic loads.

The formulation of the truss-like DEM used in this work is based on studies conducted by Nayfeh and Hefzy (1978). The objective of that work was to determine the properties of an equivalent orthotropic elastic continuum to model panels made of large numbers of small interconnected bars. Using the opposite approach, this is, to represent an orthotropic continuum using a regular truss lattice (see the concept of inverse homogenization proposed by Sigmund, 1994), the results due to Nayfeh and Hefzy (1978) were used by other authors to develop truss-like DEMs for solid mechanics problems. In this way, there have been introduced applications of truss-like DEMs to model shells subjected to impulsive loading (Riera and Iturrioz, 1995 and 1998); fracture of elastic foundations on soft sand beds (Schnaid et al, 2004); dynamic fracture (Miguel et al, 2010); generation and spread of earthquakes (Dalguer et al, 2001); scale effect in concrete (Rios and Riera, 2003) and in rocks dowels (Miguel et al, 2008 and Iturrioz et al, 2009); and the computation of fracture parameters (Kosteski et al, 2010).

In this work, a truss-like DEM is further developed to deal with ductile damage and fracture-mechanics problems. To this end, three novel features are introduced: a tri-linear elasto-plastic constitutive law; a methodology for crack discretization and the computation of stress intensity factors; and a methodology for the computation of the stress field components from the traction/compression discrete element results. The proposed methodologies are verified by solving three demanding application examples involving static and dynamic load cases.

### The Truss-like Discrete Element Method

The truss-like DEM used in this work represents the continuum by means of a periodic spatial arrangement of bars with the masses lumped at their ends. The discretization strategy is due to Nayfeh and Hefzy (1978) and it is shown in Figures 1a and 1b. The discretization uses a basic cubic module constructed using 20 bar elements and 9 nodes. Every node has three degrees of freedom, which are the three components of the displacement vector in the global reference system.

In the case of an isotropic elastic material, the equivalent axial stiffness per unit length of the longitudinal elements (those located along module edges and those connecting the nodes in the centre of the modules) is

$$E_l^A = A_l E = \phi E L^2, \quad (1)$$

where  $A_l$  is the cross-sectional area of the element,  $L$  is the length of the basic cubic module, and  $E$  is the Young's modulus of the solid being discretized. The function  $\phi = (9 + 8\delta)/(18 + 24\delta)$ , where  $\delta = 9\nu/(4 - 8\nu)$ , accounts for the effect of the Poisson's ratio  $\nu$  (see Nayfeh and Hefzy, 1978; and Dalguer et al, 2001).

Similarly, the axial stiffness per unit length of the diagonal elements is

$$E_d^A = A_d E = \frac{2}{\sqrt{3}} \delta \phi E L^2. \quad (2)$$

The coefficient  $2/\sqrt{3}$  in equation (2) accounts for the difference in length between the longitudinal and the diagonal elements, this is,  $L = 2/\sqrt{3} \cdot L_d$ .

It is important to point out that for  $\nu = 0.25$ , the correspondence between the equivalent discrete solid and the isotropic continuum is complete. On the other hand, discrepancies appear in the shear terms for values of  $\nu \neq 0.25$ . These discrepancies are small and may be neglected in the range  $0.20 \leq \nu \leq 0.30$ . For values outside this range, a different array of elements for the basic module should be used (see Nayfeh and Hefzy, 1978). It is interesting to note that while no lattice model can exactly represent a locally isotropic continuum, it can also be argued that no perfect locally isotropic continuum exists in practical engineering applications. Isotropy in solids is a bulk property that reflects the random distribution of the orientation of the constituent elements. A comprehensive study on the effect of the DEM lattice geometry on the value of the Poisson's ratio can be found in Rinaldi et al (2008).

The method is assembled by enforcing the second Newton's law at every node in the model. This procedure results in the system of equations

$$\mathbf{M} \ddot{\mathbf{x}} + \mathbf{C} \dot{\mathbf{x}} + \mathbf{F}(t) - \mathbf{P}(t) = 0 \tag{3}$$

where  $\mathbf{x}$ ,  $\dot{\mathbf{x}}$  and  $\ddot{\mathbf{x}}$  are vectors containing the nodal displacements, velocities and accelerations; and  $\mathbf{M}$  and  $\mathbf{C}$  are the mass and the damping matrices, respectively. The vectors  $\mathbf{F}(t)$  and  $\mathbf{P}(t)$  contain the internal and external nodal loads respectively.

Since matrices  $\mathbf{M}$  and  $\mathbf{C}$  are diagonal, the equations in expression (3) are not coupled, and they can be easily integrated in the time domain using an explicit finite difference scheme. It is worth noting that since nodal coordinates are updated at every time step, large displacements are accounted for naturally.

Following the Courant–Friedrichs-Lewy (CFL) criterion (see for example Bathe, 1996), the stability of the integration scheme is ensured by limiting the size of the time step. For the present implementation, the elements in the worst condition (this is, those requiring the smallest  $\Delta t$ ) are the diagonal ones. Thus, considering the relationships in Equations (1) and (2), the limitation to the time increment is

$$\Delta t \leq \frac{0.6L}{C_p} \quad (4)$$

where  $C_p$  is the propagation velocity of the longitudinal wave,

$$C_p = \sqrt{E/\rho}. \quad (5)$$

The convergence of DEM for linear elasticity and elastic instability was verified by Hayashi (1982).

The truss-like DEM has a natural ability to model cracks. They can be introduced into the models as pre-existent features and as the irreversible effect of crack nucleation and propagation. Pre-existent cracks are modelled using a simple strategy which consists in the duplication of the nodes located on the crack surface together with the elimination of the elements connecting the material on both sides of the crack. In this way, the DEM discretization is allowed to “open” along the crack locus, and pre-existent cracks are integrated seamlessly into the DEM formulation. Crack nucleation and propagation make use on non-linear constitutive models for material damage which allow the elements to break when they attain a critical condition. The details about the formulation and implementation of these non-linear constitutive models are given in the next section.

## Non-linear constitutive models for material damage

### *The bi-linear model*

Rocha et al (1991) extended the truss-like DEM by Nayfeh and Hefzy (1978) to handle fragile fracture. To this end, he introduced the bilinear constitutive relationship illustrated in Figure 1c. This constitutive law aims to capture the irreversible effects of crack nucleation and propagation by accounting for the reduction in the element load carrying capacity. The area under the force vs strain curve (the area of the triangle OAB in Figure 1c) is the energy density necessary to fracture the area of influence of the element. Thus, for a given point  $P$  on the force vs strain curve, the area of the triangle OPC represents the reversible elastic energy density stored in the element, while the area of the triangle OAP is the dissipated fracture energy density. Once the damage energy density equals the fracture energy, the element fails and loses its load carrying capacity. On the other hand, in the case

of compressive loads the material behaves as linear elastic. Thus, the failure in compression is induced by indirect traction. This assumption is reasonable for quasi fragile materials for which the ultimate strength in compression is usually from five to ten times larger than that in tension (see Kupfer and Gerstle, 1973).

Constitutive parameters and symbols in Figure 1c are (see Rocha et al, 1991; and Riera and Rocha, 1989):

- *Force,  $F$* : the element axial force as a function of the longitudinal strain  $\varepsilon$ .
- *Element stiffness,  $E_i^A$* : depending whether a longitudinal or a diagonal element is considered the values for  $E_l^A$  or  $E_d^A$ , see equations (1) and (2), should be adopted.
- *Length of the DEM module,  $L$* .
- *Specific fracture energy,  $G_f$* : the fracture energy by unit area, which is coincident with the material fracture energy,  $G_c$ .
- *Element area,  $A$* : depending whether a longitudinal or a diagonal element is considered the values for  $A_l$  or  $A_d$ , should be adopted.
- *Equivalent fracture area,  $A_i^f$* : this parameter enforces the condition that the energy dissipated by the fracture of the continuum material and its discrete representation are equivalent. With this purpose, a cubic sample with dimensions  $L \times L \times L$  is considered. The energy dissipated when a continuum sample fractures into two parts due to a crack parallel to one of its faces is

$$\Gamma = G_f \Delta = G_f L^2, \quad (6)$$

where  $\Delta$  is the fracture area. On the other hand, the energy dissipated when the DEM module fractures in two parts has to account for the contribution of five longitudinal elements (four coincident with the module edges and one internal one) and four diagonal elements, see Figure 1a. Then, the energy dissipated by a DEM module can be written as follows



$$\Gamma_{\text{DEM}} = G_f \left( 4 \cdot 0.25 \cdot c_A + c_A + 4 \cdot c_A \cdot \left( \frac{2}{\sqrt{3}} \right)^2 \right) L^2, \quad (7)$$

where the first term in the sum accounts for the four edge elements, the second term accounts for the internal longitudinal element, and the third term considers the contribution of the four diagonal elements. It is worth noting that the coefficient 0.25 in the first term accounts for the general case of an internal module with its four edge elements shared with four neighbour modules. When dealing with modules on the model surface, some of the edge elements could be shared by two elements or not shared at all. For such cases expression (7) has to be modified accordingly.

The coefficient  $c_A$  in equation (7) is a scaling parameter used to enforce the equivalence between  $\Gamma$  and  $\Gamma_{\text{DEM}}$ . Thus, equating expressions 6 and 7 results

$$G_f L^2 = G_f \left( \frac{22}{3} c_A \right) L^2, \quad (8)$$

from which it can be easily deduced that  $c_A = 3/22$ . Finally, the equivalent transverse fracture area of the longitudinal elements is

$$A_l^f = (3/22) L^2, \quad (9)$$

while for the diagonal elements is

$$A_d^f = (4/22) L^2. \quad (10)$$

- *Critical failure strain ( $\varepsilon_p$ )*: the maximum strain attained by the element before damage initiation (point A in Figure 1c). The relationship between  $\varepsilon_p$  and the specific fracture energy,  $G_f$ , is given in terms of Linear Elastic Fracture Mechanics concepts. In this way

$$\varepsilon_p = R_f \sqrt{\frac{G_f}{E(1-\nu^2)}}, \quad (11)$$

where  $R_f$  is the so-called failure factor, which accounts for the presence of an intrinsic defect of size  $d$ .  $R_f$  is defined as

$$R_f = \frac{1}{Y\sqrt{d}}, \quad (12)$$

where  $Y$  is a dimensionless parameter that depends on both the specimen and the crack geometry.

It is worth noting here that the intrinsic defect size,  $d$ , is predetermined, and it could be consider as a material property.

Any disorder in the material properties is introduced to the model by specifying a random distribution in the specific fracture energy,  $G_f$ .

- *Limit strain* ( $\varepsilon_r$ ): the strain value for which the element loses its load carrying capacity (point C in Figure 1c). This value must be set to satisfy the condition that, upon the failure of the element, the dissipated energy density equals the product of the element influence area,  $A_i^f$ , times the specific fracture energy,  $G_f$ , divided by the element length. This is

$$\int_0^{\varepsilon_r} F(\varepsilon) d\varepsilon = \frac{G_f \cdot A_i^f}{L_i} = \frac{K_r \cdot \varepsilon_p^2 \cdot E \cdot A_i}{2} = \frac{K_r \cdot \varepsilon_p^2 \cdot E_i^A}{2}, \quad (13)$$

where the sub indexes  $i$  have to be specialized to  $l$  or  $d$  depending whether the element under consideration is a longitudinal or diagonal one, respectively.

The coefficient  $K_r$  in equation (13) is a function of the material properties and the element length,  $L_i$ . Recalling the first equality in Equation (1) and substituting it into equation (13), the expression for  $K_r$  can be retrieved:

$$K_r = \left( \frac{G_f}{E \varepsilon_p^2} \right) \left( \frac{A_i^f}{A_i} \right) \left( \frac{2}{L_i} \right). \quad (14)$$

In order to guarantee the stability of the algorithm, the condition  $K_r \geq 1$  must be accomplished (Riera and Rocha, 1991). In this sense it is interesting to define the critical element length

$$L_{cr} = 2 \left( \frac{G_f}{E \varepsilon_p^2} \right) \left( \frac{A_i^f}{A_i} \right). \quad (15)$$

The coefficient  $\left( \frac{A_i^f}{A_i} \right)$  in equation (15) is  $\left( \frac{A_l^f}{A_l} \right) = \frac{3}{22\phi}$  and  $\left( \frac{A_d^f}{A_d} \right) = \frac{\sqrt{3}}{11\delta\phi}$  for the longitudinal and diagonal elements respectively (see equations (1), (2), (9) and (10)). In the special case of an isotropic continuum with  $\nu=0.25$ , the value of the functions  $\delta=1.125$

and  $\phi=0.4$ , which results in  $\left(\frac{A_l^f}{A_l}\right)=\left(\frac{A_d^f}{A_d}\right)\approx 0.34$ . Thus, for practical purposes a single value of the critical element length can be used for both the longitudinal and diagonal elements. Therefore, the above stability condition can be expressed as

$$K_r = \frac{L_{cr}}{L_i} \geq 1 \Rightarrow L_i \leq L_{cr}. \quad (16)$$

This is, there is a maximum element length which preserves the stability of the element constitutive relationship.

Finally, the expression for the limit strain is

$$\varepsilon_r = K_r \varepsilon_p. \quad (17)$$

It is interesting to note that in contrast to the usual practice in finite and boundary elements, the constitutive relationship in the DEM is not a function of the material properties only. The element constitutive relationship introduced above is defined in terms of parameters which are material properties ( $\varepsilon_p$ ,  $E$ ,  $R_{fc}$  and  $G_f$ ), depend on model discretization ( $A_i^f$  and  $L$ ) and depend on both, the material properties and the model discretization ( $E_i^A$  and  $\varepsilon_r$ ). Besides, it is worth noting that although the DEM uses a scalar damage law to describe the uniaxial behaviour of the elements, the global model accounts for anisotropic damage since it possess elements orientated in different spatial directions.

### *The tri-linear model*

The bi-linear element constitutive relationship described in the previous section is extended in this section to account for elasto-plastic behaviour by introducing the tri-linear constitutive relationship illustrated in Figure 1d. For a given point  $P$  on the force vs strain curve, the area of the triangle  $O'PC$  represents the reversible elastic energy density stored in the element, while the area of the polygon  $OAA'PO'$  corresponds to the dissipated energy density. The dissipated energy is associated not only with the fracture energy as in the bi-linear model, but also with the energy dissipation due to the plastic deformation. In addition to the parameters introduced for the bilinear element constitutive relationship, the

definition of the tri-linear law uses two extra parameters, namely  $\varepsilon_p'$  and  $E_i^{A'}$  (see Figure 1d).

The behaviour in compression is the same to that in tension.

The element failure occurs when the dissipated energy density (area  $OAA'PO'$  in Figure 1d) equals the total area under the force vs displacement plot (area  $OAA'B$ ). This is

$$\int_0^{\varepsilon_r} F(\varepsilon) d\varepsilon = \frac{G_f A_i^f}{L_i} = \frac{\varepsilon_p^2 E_i^A}{2} + (\varepsilon_p' - \varepsilon_p) \varepsilon_p E_i^A + \frac{(\varepsilon_p' - \varepsilon_p)^2 E_i^{A'}}{2} + \frac{(\varepsilon_r - \varepsilon_p')(\varepsilon_p E_i^A + (\varepsilon_p' - \varepsilon_p) E_i^{A'})}{2} \quad (18)$$

where the four summands in the last member account for the total area under the force vs strain diagram depicted in Figure 1d. Following a similar approach to that for the bi-linear model, it is possible to obtain the value for the factor  $K_r'$  that relates the strain  $\varepsilon_p'$  with the limit strain,  $\varepsilon_r$ :

$$\varepsilon_r = K_r' \varepsilon_p'. \quad (19)$$

The expression for  $K_r'$  results from equation (18) and it yields

$$K_r' = \frac{\frac{2G_f A_i^f}{L_i \varepsilon_p'} + \frac{\varepsilon_p^2}{\varepsilon_p'} (E_i^A - E_i^{A'}) + 2E_i^{A'} \varepsilon_p}{(\varepsilon_p (E_i^A - E_i^{A'}) + \varepsilon_p' E_i^{A'})} - 1. \quad (20)$$

The stability of the tri-linear element constitutive relationship is ensured by means of two conditions:

$$\varepsilon_p' \geq \varepsilon_p \quad \text{and} \quad (21)$$

$$K_r' \geq 1.$$

### Computation of stresses

The visualization of the stress contours is a key tool to assess the performance of a numerical model. Since the stress fields are not a direct outcome for the DEM used in this work, a simple post processing methodology was devised for the computation of the stresses from the uniaxial element results.

Stresses are assumed constant over each DEM module, and the components of the stress tensor are computed as the ratio between the mean equivalent resultant force,  $F_{eq}$ , and the cross section of the module. The mean equivalent resultant force is computed from the individual forces exerted by the module elements,  $F_n$ . The procedure for the computation of the normal and shear stress components  $\sigma_{11}$  and  $\sigma_{12}$  are given in Tables 1 and 2. Analogous procedures are used for the remaining stress components.

The performance of the proposed methodology was assessed by comparison with results computed using the Finite Element Method (FEM). These analyses were carried out on a series of randomly generated models for a ferritic cast iron microstructure. This problem will be described in the detail in one of the examples presented later in this paper. By now it is only mentioned here that the model geometry consists of a metal matrix with circular graphite nodules. The graphite nodules of radius  $r=25\text{ }\mu\text{m}$  are randomly distributed over the problem domain, and they can be assimilated to voids because they possess very weak mechanical properties when compared to the metal matrix.

The DEM discretization for a typical model is illustrated in Figure 2b. The element length was chosen four times smaller than the nodule radius, this is,  $L/r=0.25$ . Based on previous results (see Galiano, 2007), the model discretization used two modules in the direction of the thickness. That discretization strategy was found appropriate to reproduce the plane stress condition. The resulting discretization consisted of 4800 modules with approximately 29000 degrees of freedom. On the other hand, FEM models were constructed using approximately 16000 4-noded quadrilateral elements (PLANE 42 element), see Figure 2a. FEM models were solved using ANSYS 7 (2007).

DEM and FEM results were compared along a number of paths which were regularly placed on the sample domains (see Figure 2). As an example, FEM and DEM results for the von Misses equivalent stress along the path #6 of the example in Figure 2 are plotted in Figure 3a. Figure 3b presents the histogram with the distribution of the error (the difference between the DEM and FEM results) for the 485 positions evaluated along the nine paths shown in Figure 2. Mean value for the error is 0.47%, with a standard deviation of around 7%. A comprehensive report of the obtained results for the complete set of models and other benchmark tests are reported in Galiano et al (2003). Based on that results, it was concluded that the proposed procedure possess a reasonable accuracy for assessing the

DEM results using contour plots. Contour plots will be illustrated for the examples in the next section.

**Computation of stress intensity factors**

The stress intensity factors (SIFs) are computed by replacing the DEM displacement results into the theoretical expressions for the displacement fields near the crack tip. This is a common procedure used with finite and boundary element methods. The mixed-mode SIFs can be written in terms of the displacement fields in the vicinity of the crack tip as follows (see for instance Aliabadi and Rooke, 1991 or Anderson, 2005):

$$\begin{aligned} K_I &= u_y \frac{E}{8} \sqrt{\frac{2\pi}{r}}, \\ K_{II} &= u_x \frac{E}{8} \sqrt{\frac{2\pi}{r}}, \\ K_{III} &= u_z \frac{E}{8} \sqrt{\frac{2\pi}{r}}, \end{aligned} \tag{22}$$

where  $u_x$ ,  $u_y$  and  $u_z$  are the components of the relative displacement between the crack surfaces measured at a distance  $r$  from the crack tip (see Figure 4).

In the present implementation, the relative displacement between the crack surfaces,  $u$ , are measured at a number of positions,  $r$ , coincident with the nodes of the DEM discretization. These displacements are replaced into equations (22) to compute their corresponding sets of values for  $K_I(r)$ ,  $K_{II}(r)$  and  $K_{III}(r)$ . Finally, the SIFs,  $K_I$ ,  $K_{II}$  and  $K_{III}$ , result from the linear extrapolation of the  $K(r)$  values for  $r \rightarrow 0$ . The coefficients for the extrapolation are computed using least square fitting. It is worth mentioning that, being the SIF a local parameter, the proposed procedure is suitable for the analysis of both, static and dynamic crack problems.

**Examples**

There are presented in this section three validation examples devoted to verify and to illustrate the performance of the proposed implementations. It is worth noting that although the DEM presented in this paper is three-dimensional, the examples are two-dimensional.

The reason for the selection of such examples was to allow the comparison of the results to those available in the literature.

### *Slant crack in a rectangular plate under impact loading*

This example consists in the computation of the dynamic stress intensity factor for a 45° inclined crack in a rectangular plate. The problem geometry and dimensions are given in Figure 5a. The plate was dynamically excited by a uniform impact traction,  $\sigma_0$ , in the vertical direction. The load was specified using a Heaviside function at time  $t = 0$ . The plate had a linear elastic behaviour. Material properties were:  $E = 200$  GPa,  $\nu = 0.3$ ,  $\rho = 5000$  kg/m<sup>3</sup>. The material fracture toughness was set high enough to avoid crack propagation. The DEM model was discretized using a 150×300×1 module mesh in the directions of the specimen width, height and thickness, respectively. The model module length was  $L = 2 \cdot 10^{-4}$  m. The model consisted in approximately 90000 degrees of freedom. The nodal displacements in the direction of the thickness were constrained in order to impose the plane strain condition to the model. Previous results (see Galiano, 2007) showed that this discretization strategy accurately reproduces the plane strain condition.

Figure 5b depicts the details of the procedures for the application of the load and the crack modelling. The load was applied to the central node of the modules located next to the bottom and top edges of the plate. The geometry of the crack was approximated using a relatively fine (one twentieth of the crack length) zigzag pattern. The problem was solved using  $\Delta t = 1 \times 10^{-8}$  second time increments.

The evolution in time of the mixed-mode dynamic stress SIFs,  $K_I$  and  $K_{II}$ , are plotted in Figure 6. In every case the SIF results are normalized with respect to  $K_0 = \sigma_0 \cdot \sqrt{\pi \cdot a}$ . Results in Figure 6 are compared to those due to Dominguez and Gallego (1992) who solved the problem using the Boundary Element Method (BEM) in the time domain and due to Krysl and Belytschko (1999) who used the element-free Galerkin method. There exists a good agreement between the three sets of results.

Figure 7 depicts a series of stress contour plots for the maximum principal stress at  $t = 3, 6, 9, 12, 15$  and  $18 \mu s$ . It can be observed that before the arrival of the longitudinal stress wave to the crack tip, this is for  $t < 3.6 \mu s$ , both the stress at the crack tip (see Figure 7a), and

consequently the SIF values (see Figure 6) are zero. Afterwards, the stress level starts increasing (see Figures 7b to 7d) together with the SIF values (see Figure 6). The maximum  $K_{II}$  occurs at  $t = 9.5 \mu\text{s}$ , while  $K_I$  is nearly constant during the period  $9.5 \mu\text{s} < t < 12 \mu\text{s}$  (see Figure 6). After this moment, both the stress level at the crack tips and the SIF values diminish following the trend indicated in the figures.

### ***Dynamic crack propagation: the Kalthoff- Winkler experiment***

In the Kalthoff-Winkler (1988) experiment a specimen with two parallel edge cracks was impacted by a projectile with a diameter equal to the distance between the two cracks (see Figure 8a). No displacement restrictions were prescribed to the specimen. The specimen material was polymethylmethacrylate (PMMA) with the following properties  $E = 190 \text{ GPa}$ ,  $\nu = 0.30$ ,  $G_c = 22170 \text{ N/m}$ ,  $\sigma_u = 844 \text{ MPa}$  and  $\rho = 8000 \text{ Kg/m}^3$ . The velocity of the projectile was  $16.5 \text{ m/s}$ .

The above experiment was simulated using then DEM model illustrated in Figure 8b. Due to the problem symmetry, only one half of the specimen was discretized. The appropriate displacement boundary conditions were applied along the bottom edge of the model. Following the same discretization strategy used for the previous example, the DEM model was discretized using a  $40 \times 40 \times 1$  module mesh in the directions of the width, the height and the thickness, respectively. The discretized model consisted in approximately 9400 degrees of freedom. The nodal displacements in the direction of the thickness were constrained in order to impose the plane strain condition. The details in Figure 8b illustrate the strategy used to prescribe the displacements along the bottom edge of the specimen and the velocity in the impact zone. The crack was modelled using the same approach of the previous example; this is, by deleting elements and duplicating nodes along the crack locus. Being the PMMA a brittle material, the bilinear constitutive law (see Figure 1c) was assigned to all the elements in the model. The DEM model parameters were  $L = 2.5 \times 10^{-3} \text{ m}$ ,  $G_f = 22170 \text{ N/m}$ ,  $\nu = 0.25$ ,  $\varepsilon_p = 0.00444$ , and  $\Delta t = 1 \times 10^{-7} \text{ seconds}$ .

Figure 9a depicts the resulting crack path geometry. It can be observed that the obtained result is in close agreement to those computed by Belytschko et al (2003) using XFEM and by Huespe et al (2006) using the strong discontinuity approach and FEM (see Figures 9b and 9c, respectively). In every case not only the pre-existent crack propagates, but also a



new crack nucleates and propagates from the opposite side to that where the projectile impacted.

The DEM results were post processed to compute the crack propagation velocity of the pre existent crack. This was done by recording the crack tip position as a function of time for a series of snapshots of the DEM simulation. The result is plotted in Figure 10, together with the results reported by Belytschko et al (2003) and Huespe et al (2006). The agreement between the three sets of results is reasonably good. It can be observed that the three models predict the start of the crack propagation in the range  $24\mu\text{s} < t < 25\mu\text{s}$ . Besides, the mean crack velocity in the early stages of the crack propagation (say up to  $t \approx 50\mu\text{s}$ ) for the DEM model is  $V_{\text{DEM}} \approx 1600\text{ m/s}$ , what is around 10% to 15% lower than those reported by the references. Finally, it is noted that the mean propagation velocity resulting from the three models is always bellow the theoretical limit, the Raleigh wave velocity,  $V_{\text{R}} = 2799\text{ m/s}$  (see Freund, 1989).

### ***Damage-mechanics analysis of a nodular cast iron microstructure***

Nodular cast iron microstructure consists in dispersed graphite spheroids (nodules) in a ferrous matrix, which can spread from purely ferritic to perlitic. Mechanical properties of nodular cast iron vary in a wide range of values, mostly controlled by the effect of the nodule size and distribution, together with the process of microcrack nucleation, growth and coalescence (see Berdin et al, 2001; Bonora and Ruggiero, 2005; Basso et al, 2009).

It is presented in this example the application of the DEM to model the micromechanics of failure of a nodular cast iron. While a number of authors (see for example Bonora and Ruggiero, 2005) have studied this problem using periodic unit-cell models, it is proposed in this work to use representative volume elements (RVE). RVEs consist of a homogeneous isotropic metal matrix with twenty randomly distributed graphite nodules. The details of the studies concerning the topological analysis of the microstructure and the determination of the RVE size can be found in the works by Ortiz et al (2001) and Galiano et al (2007).

The mechanical properties of the cast iron were those reported by Berdin et al (2001):  $E=187\text{ GPa}$ ,  $\sigma_y=260\text{ MPa}$ ,  $\sigma_{\text{UTS}}=390\text{ MPa}$ , total elongation 19%,  $K_{\text{IC}}=77\text{ MPa}\cdot\sqrt{\text{m}}$ . The nodule volume fraction was 7.7%. Nodules were introduced into the DEM model by setting the graphite mechanical properties to those elements with their centroids located within the

nodules loci. A typical model discretization is illustrated in Figure 2b, where the elements in the locus of the nodules had been deleted in order to better visualize the model. The mechanical properties of graphite were set as follows: Young's modulus:  $E = 15$  GPa, Poisson coefficient  $\nu = 0.3$ , fracture toughness  $K_{IC} = 1$  MPa $\cdot\sqrt{\text{m}}$ , tensile strength  $\sigma_{ut} = 25$  MPa. Graphite exhibits a brittle behaviour and thus it was modelled using the bilinear constitutive relationship with the following data for the constitutive parameters (see Figure 1c):  $\varepsilon_p = 1.66 \times 10^{-3}$ ,  $\varepsilon_r = 2.67$ ,  $E = 15 \times 10^9$  N/m<sup>2</sup>,  $G_f = 67$  N/m.

The ductile behaviour of the metal matrix was modelled using the trilinear constitutive law (see Figure 1d). The parameters for the **element constitutive relationship** were adjusted to reproduce the macroscopic stress vs strain behaviour of the cast iron reported by Berdin et al (2001). The resulting material properties for the matrix material were:  $E = 233$  GPa and  $\sigma_y = 325$  MPa, which compare well to the values  $E = 210$  GPa and  $\sigma_y = 325$  MPa reported by Bonora and Ruggerio (2005). The associated parameters for the **element constitutive relationship** were:  $\varepsilon_p = 9.2 \times 10^{-4}$ ,  $\varepsilon'_p = 0.229$ ,  $\varepsilon_r = 5.894$ ,  $E = 2.5 \times 10^{11}$  N/m<sup>2</sup>,  $G_f = 11 \times 10^3$  N/m and  $L = 3.33 \times 10^{-6}$  m. **The model discretization strategy is that discussed in the section Computation of Stresses.**

Uniaxial traction tests were modelled for twenty randomly generated RVEs and a periodic microstructure. Stress vs strain results are presented in Figure 11 together with the experimental results from Berdin et al (2001). The results for the RVE analyses are reported using the mean value of the twenty samples and their standard deviation.

It can be observed in Figure 11 the difference in the behaviour between the RVE models and their periodic counterparts. The periodic models exhibit a constant strain hardening in contrast to the softening observed of the RVE models and the experimental data. In an attempt to provide a further insight to better understand this difference, the sequence of subfigures in Figure 11 depict the evolution of the damage with the applied load for a typical RVE. Black areas in the subfigures correspond to those **with plastic deformation**. Subfigure (a) shows the localization of damage in the ligaments between the nodules in the early stages of the non-linear portion of the stress vs strain curve. Damage localization progresses with the increment of the load up the point where coalescence starts. This phenomenon is illustrated in subfigure (b) for the case of two nodules merging in a single

void (see circled detail). Finally, subfigure (c) depicts the stage of advanced damage, with void growth and coalescence extensively spread over the specimen domain. These last phenomena results in the rapid loss of the load carrying capacity. On the other hand, the periodic distribution of the nodules conducts to the simultaneous failure of all the matrix ligaments between the nodules (see subfigure d), avoiding the damage localization to occur like in the RVE models.

Figure 12 presents the evolution of the elastic and dissipated energy densities as functions of the longitudinal strain. These results can be easily computed from the DEM model by adding up the individual contributions of the elements (the area  $O'PC$  for the reversible elastic energy density and the area  $OAA'PO'$  for the dissipated energy density, see Figure 1d). It can be seen that both, the elastic and dissipated energy densities are higher for the periodic model than for the RVE. This result could look contradictory if we consider that RVE models fail at a lower stress level than their periodic counterpart. However, the explanation for such behaviour can be given in terms of damage localization. The periodic model spreads the damage over the complete model domain, and thus, it dissipates more damage energy before failure than the RVE which leads to the formation of a crack. This result emphasizes the key role played by the random spatial distribution of nodules when assessing the nonlinear behaviour of the material. This limitation for the periodic model is in agreement with results presented by other authors who studied the problem using FEM (see for example Kousnetsova, 2001 and Pierard et al, 2007).

## Conclusions

It has been presented in this paper a customization of a truss-like discrete element method with the objective of further extend its capabilities to solve fracture and damage mechanics problems. The novel features are: the formulation of elasto-plastic element constitutive relationship and procedures for the computations of stresses and stress intensity factors.

The performance of the proposed methods has been assessed by solving three challenging application examples. In every case, the computed results helped understanding the mechanics of failure in terms of stress intensity factors, energy balance, damage localization and stress results. The computed results were in every case in good agreement with the experimental and numerical results reported in the literature.

The obtained results show that the truss-like DEM introduced in this work constitutes a simple and versatile numerical tool to deal with fracture and damage mechanics problems. The method can be effectively used for the analysis of problems in terms of the energy balance, stress intensity factors and damage patterns. On the other hand, the accuracy of the stress results is lower than those which could be computed using FEM or BEM. However, the DEM stress results are fairly precise for visualization purposes.

The proposed method can be easily extended to deal with other damage mechanisms like creep, time dependent degradation and coupled damage-plastic behaviours. Besides, the versatility of the DEM could be exploited by coupling it to finite or boundary element methods. Such a coupling strategy would allow using the discrete element method to represent those regions of the model undergoing localized damage, while finite or boundary elements are used to deal with the undamaged regions.

### Acknowledgments

The authors acknowledge the support of CNPq and CAPES (Brazil) and the Agencia Nacional de Promoción Científica y Tecnológica (Argentina).

### References

- Absi, E. (1971). "Théorie des equivalences-determination de quelques éléments types", *Proceedings of L'institut Technique Du Balument el des Travau Publics*, N° 281, pp. 83-86.
- Aliabadi M.H. and Rooke D.P. (1991), "*Numerical Fracture Mechanics*", Computacional Mechanics Publications and Kluwer Academic Publishers, Southampton, UK.
- Anderson T.L. (2005), "*Fracture Mechanics. Fundamentals and Applications*", CRC Press, Boca Ratón, USA.
- Belytschko, T., Chen, H., Xu, J. and Zi, G. (2003), "Dynamic crack propagation based on loss of hyperbolicity and a new discontinuous enrichment", *International Journal for Numerical Methods in Engineering*, Vol. 58, pp 1873-1905.
- Basso, A., Martínez, R., Cisilino, A.P. and Sikora, J. (2009), "Experimental and numerical assessment of crack propagation in dual-phase austempered ductile iron", *Fatigue and Fracture of Engineering Materials and Structures*, Vol 33, pp. 1-11.
- Bathe, K. J. (1996), "*Finite element procedures*", Prentice-Hall, Inc., New Jersey.

- 1  
2  
3 Berdin, C., Dong, M.J. and Prioul, C. (2001), “Local approach of damage and fracture  
4 toughness for nodular cast iron”, *Engineering Fracture Mechanics*, Vol. 68, pp.  
5 1107-1117.  
6  
7  
8  
9 Bonora, N. and Ruggiero, N. (2005), “Micromechanical modeling of ductile cast iron  
10 incorporating damage – Part I Ferritic Ductile Cast Iron”, *International Journal of*  
11 *Solids and Structures*, Vol. 42/5-6, pp. 1401-1424.  
12  
13  
14 Chiaia B., Vervuurt A., and Van Mier J.G. (1997), “Lattice model evaluation of progressive  
15 failure in disordered particle composites”, *Engineering Fracture Mechanics*, Vol. 57,  
16 No. 2/3, pp. 301-318.  
17  
18  
19 Cottrell M.G., Yu J. And Owen D.R.J. (2003), “The adaptive and erosive numerical  
20 modelling of confined boron carbide subjected to large-scale dynamic loadings with  
21 element conversion to undeformable meshless particles”, *International Journal of*  
22 *Impact Engineering*, Vol. 28, pp. 1017-1035.  
23  
24  
25  
26 Cundall, P.A. and Strack O.D.L. (1979). “A distinct element model for granular  
27 assemblies”, *Geotechnique*, Vol. 29:47, pp. 65.  
28  
29  
30 Dalguer, L. A., Irikura, K., Riera, J.D. and Chiu, H. C. (2001), “The importance of the  
31 dynamic source effects on strong ground motion during the 1999 Chi-Chi, Taiwan,  
32 earthquake: brief interpretation of the damage distribution on buildings”, *Bulletin of*  
33 *the Seismological Society of America*, Vol. 91/5, pp. 1112–1127.  
34  
35  
36  
37 Dominguez, J. and Gallego, R. (1992), “Time domain boundary element method for  
38 dynamic stress intensity factor computations”, *International Journal for Numerical*  
39 *Methods in Engineering*, Vol. 33, pp. 635-647.  
40  
41  
42 Freund, L. B. (1989), “*Dynamic Fracture Mechanics*”, Cambridge University Press,  
43 Cambridge, UK.  
44  
45  
46 Galiano Batista, R., Iturrioz, I., and Cisilino, A.P. (2003), “Computation of stresses and  
47 strains using the discrete element method”, *XXIV Iberian Latin-American Congress*  
48 *on Computational Methods in Engineering (CILAMCE 2003)*, Ouro Preto, Brazil,  
49 2003 (in Portuguese).  
50  
51  
52  
53 Galiano Batista R. (2007), “*Application of the Discrete Element Method to Study the*  
54 *Damage Micromechanics of Microporous Metallic Materials*”, PhD thesis,  
55 Universidade Federal do Rio Grande do Sul, Brazil (in Portuguese).  
56  
57  
58  
59  
60

Fraternali F., Angelillo M. And Fortunato A. (2002), "A lumped stress method for plane elastic problems and the discrete-continuum approximation", *International Journal of Solids and Structures*, Vol. 39, pp. 6211-6240.

Hayashi, N. (1982), "Sobre um Modelo de discretização de Estruturas tridimensionais aplicado a dinâmica Não linear", *MSc. Thesis*, CPGEC, Universidade Federal de Rio Grande do Sul, Brazil (in Portuguese).

Huespe, A. E., Oliver J., Sanchez, P. J., Blanco, S. and Sonzogni, V. (2006). "Strong discontinuity approach in dynamic fracture simulations", *Mecánica Computacional*, Vol. 24, pp. 1997-2018.

Hrennikoff A. (1941). "Solution of problems of elasticity by the framework method", *Journal of Applied Mechanics*, Vol. 12, pp. 169-175.

Iturrioz, I., Miguel, L. F. F. and Riera, J. D. (2009), "Dynamic fracture analysis of concrete or rock plates by means of the Discrete Element Method", *Latin American Journal of Solids and Structures*, Vol. 6, pp. 229-245.

Kalthoff, J. F. and Winkler, S. (1988), "Failure mode transition at high rates of shear loading", *DGM Informationsgesellschaft mbH, Impact Loading and Dynamic Behavior of Materials*, Vol. 1, pp. 185-195.

Klerck P.A., Sellers E.J. and Owen D.R.J. (2004), "Discrete fracture in quasi-brittle materials under compressive and tensile stress states", *Computer Methods in Applied Mechanics and Engineering*, Vol. 193, pp. 3035-3056.

Kosteski, L., Barrios, R. and Iturrioz, I. (2010) "Fractomechanics parameter calculus using the Discrete Element Method", to be published in the *Latin American Journal of Solids and Structures*.

Kouznetsova, V., Brekelmans, W.A.M. and Baaijens, F.P.T. (2001), "An approach to micro-macro modeling of heterogeneous materials", *Computational Mechanics*, Vol. 27, pp. 37-48.

Krysl, P. and Belytschko, T. (1999), "The element free Galerkin method for dynamic propagation of arbitrary 3D cracks", *International Journal for Numerical Methods in Engineering*, Vol. 154, pp. 33-150.

Kupfer, H. B. and Gerstle, K. H., (1973). "Behaviour of concrete under biaxial stresses", *Journal of the Engineering Mechanics Division*, American Society of Civil



Engineers, Vol. 99, No. 4, pp. 853-866.

Miguel L.F.F., Riera J.D. and Iturrioz I. (2008), "Influence of size on the constitutive equations of concrete or rock dowels", *International Journal for Numerical and Analytical Methods in Geomechanics*, Vol. 32/15, pp. 1857 – 1881.

Miguel L.F., Iturrioz I. and Riera J.D. (2010), "Size effects and mesh independence in dynamic fracture analysis of brittle materials", *Computer Methods Modeling in Engineering & Sciences*, Vol. 56, No. 1, pp.1-16.

Munjiza, A. (2009), Guest editorial From: Engineering Computations: International Journal for Computer-Aided Engineering and Software, Vol. 26/6.

Nayfeh, A.H. and Hefzy, M.S. (1978), "Continuum modeling of three-dimensional truss-like space structures", *AIAA Journal*, Vol. 16/8, pp. 779–787.

Pierard, O., Llorca, J., Segurado, J. and Doghri, I. (2007), "Micromechanics of particle-reinforced elasto-viscoplastic composites: Finite element simulations versus affine homogenization", *International Journal of Plasticity*, Vol. 23, pp. 1041-1060.

Ortiz, J., Cisilino, A.P. and Otegui, J.L. (2001), "Effect of microcracking on the micromechanics of fatigue crack growth in austempered ductile iron", *Fatigue and Fracture of Engineering Materials and Structures*, Vol. 24/9, pp.591-606.

Riera J.D. and Iturrioz I. (1995), "Discrete element dynamic response of elastoplastic shells subjected to impulsive loading", *Communications in Num. Meth. in Eng.*, Vol. 11, pp. 417-426

Riera J.D. and Iturrioz I. (1998), "Discrete element model for evaluating impact and impulsive response of reinforced concrete plates and shells subjected to impulsive loading", *Nuclear Engineering and Design*, Vol. 179, pp. 135-144.

Riera, J. D. and Rocha, M.M. (1991), "A note on the velocity of crack propagation in tensile fracture", *Revista Brasileira de Ciencias Mecanicas*, Vol. XII/3, pp. 217-240.

Rinaldi A. and Lai Y.C. (2007), "Statistical damage theory of 2D lattices: Energetics and physical foundations of damage parameter", *International Journal of Plasticity*, Vol. 23, pp. 1769-1825.

Rinaldi A., Krajcinovic D., Peralta P. and Lai Y.C. (2008), "Lattice models of polycrystalline microstructures: A quantitative approach", *Mechanics of Materials*, Vol. 40, pp. 17–36.

Rios R.D. and Riera J.D. (2004), “Size effects in the analysis of reinforced concrete structures”, *Engineering Structures*, Vol. 26, pp. 1115-1125.

Rocha M.M., Riera J.D. and Krutzik N.J. (1991). “Extension of a model that aptly describes fracture of plain concrete to the impact analysis of reinforced concrete”, in *International Conference on Structural Mechanics Reactor Technology (SMIRT 11)*, Tokyo, Japan.

Schlangen E. and Garboczi E.J. (1997), “Fracture simulations of concrete using lattice models: computational aspects”, *Engineering Fracture Mechanics*, Vol. 57, pp. 319–332.

Schnaid F., Spinelli L., Iturrioz I. and Rocha M. (2004), “Fracture mechanics in ground improvement design”, *Ground Improvement*, Vol. 8, pp. 7-15.

Sigmund O. (1994), “Materials with prescribed constitutive parameters: An inverse homogenization problem”, *International Journal of Solids and Structures*, Vol. 31, Issue 17, pp. 2313-2329.

Slepyan L.I. (2005), “Crack in a material-bond lattice”, *Journal of the Mechanics and Physics of Solids*, Vol. 53, pp. 1295-1313.



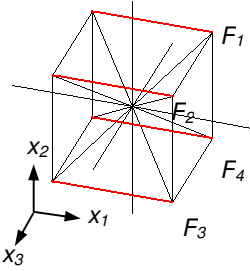
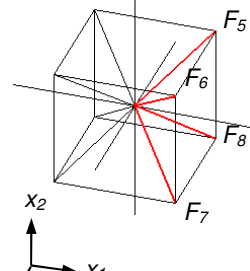
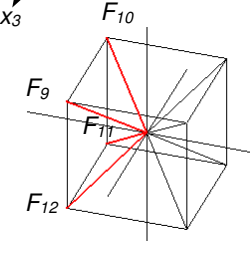
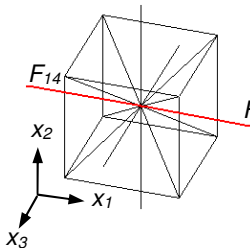
Normal stress $\sigma_{II}$		
Elements	Resultant equivalent forces	Stress
	$F_{11}^a = \frac{F_1 + F_2 + F_3 + F_4}{4}$	$\sigma_{11} = \frac{F_{11}}{A} = \frac{F_{11}^a + \frac{1}{2}(F_{11}^{b1} + F_{11}^{b2}) + F_{11}^c}{A}$ <p>A: cross section of the module</p>
 	$F_{11}^{b1} = \alpha \cdot (F_5 + F_6 + F_7 + F_8)$ $F_{11}^{b2} = \alpha \cdot (F_9 + F_{10} + F_{11} + F_{12})$ $\alpha=0.577$ : cosine of the angle given by the orientation of the diagonal elements with respect to the $x_I$ direction.	
	$F_{11}^c = \frac{F_{13} + F_{14}}{2}$	

Table 1: procedure for the computation normal stress components  $\sigma_{II}$ .

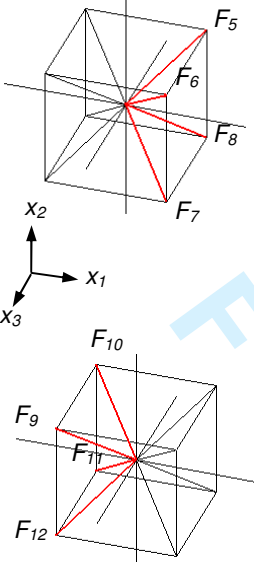
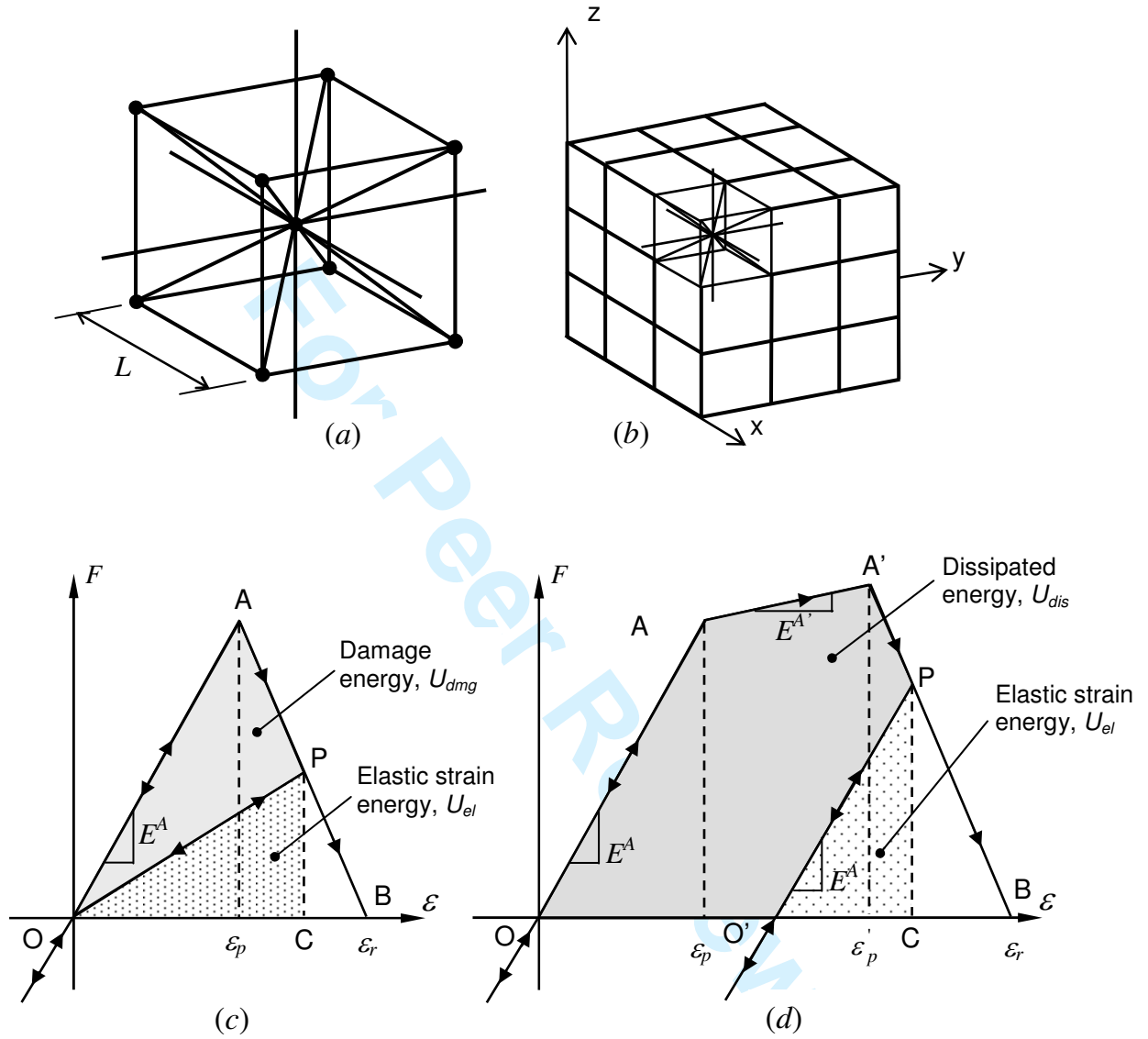
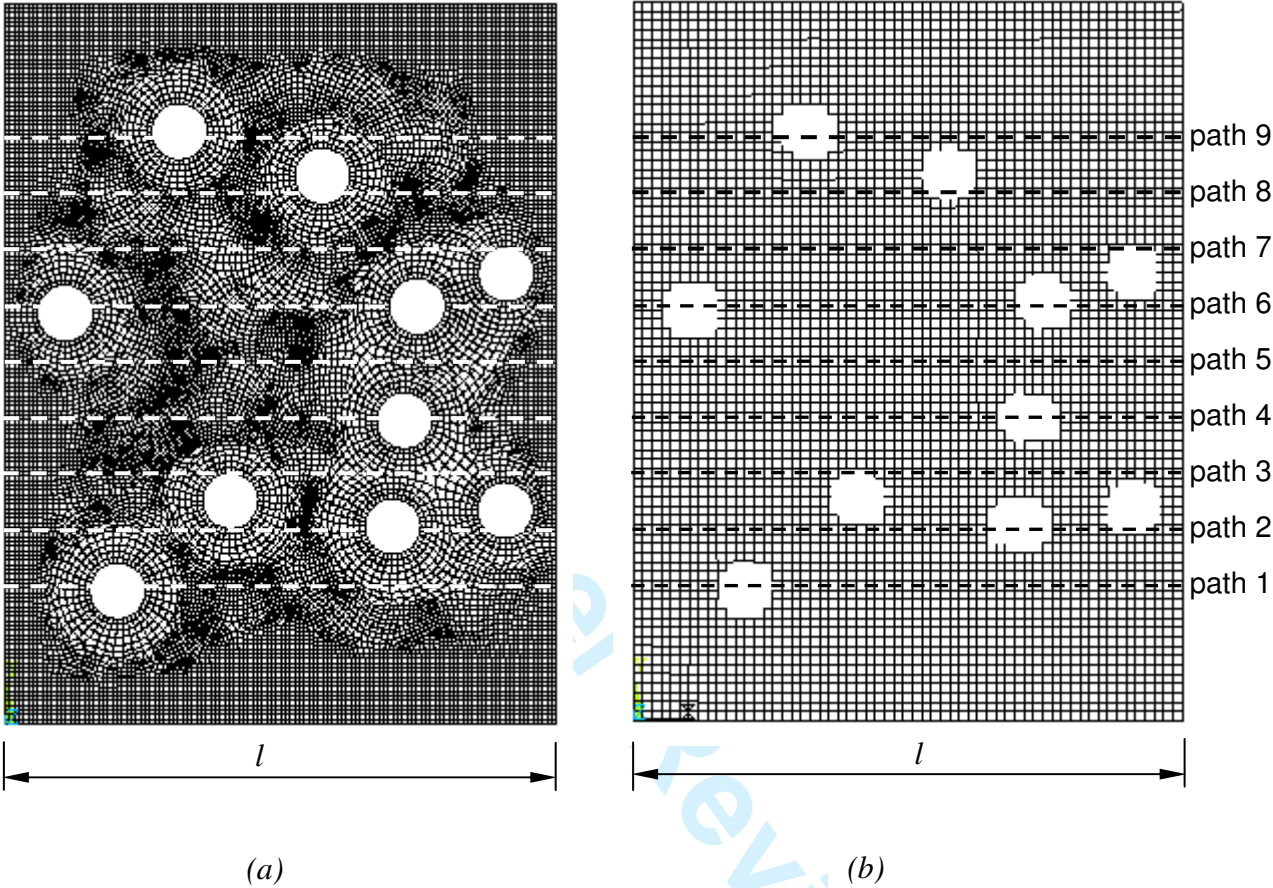
Shear stress $\sigma_{12}$		
Elements	Resultant equivalent forces	Stress
	$F_{12}^{b_1} = \frac{\alpha \cdot (F_5 - F_8) + \alpha \cdot (F_6 - F_7)}{2}$ $F_{12}^{b_2} = \frac{\alpha \cdot (F_{10} - F_{11}) + \alpha \cdot (F_9 - F_{12})}{2}$ $\alpha=0.577: \text{ cosine of the angle given by the orientation of the diagonal elements with respect to the } x_i \text{ direction.}$	$\sigma_{12} = \frac{F_{12}}{A} = \frac{\frac{F_{12}^{b_1} + F_{12}^{b_2}}{2}}{A}$  A: cross section of the module

Table 2: procedure for the computation shear stress components  $\sigma_{12}$ .



**Figure 1:** DEM discretization strategy: (a) basic cubic module, (b) generation of prismatic body, (c) bilinear and (d) trilinear constitutive models.



**Figure 2:** (a) FEM and (b) DEM discretizations. For the sake of clearness only the longitudinal elements are plotted in the DEM discretization. The paths are those used to compare the FEM and DEM results.

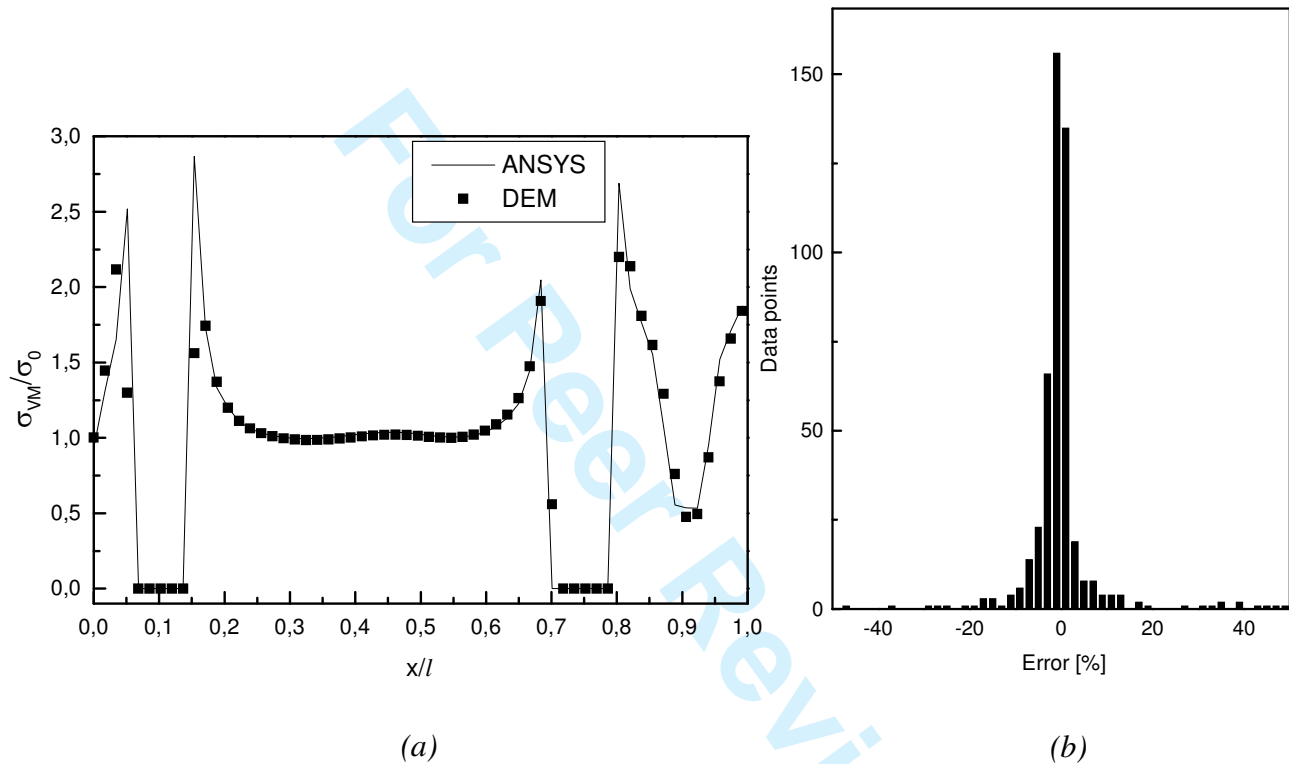


**Figure 3:** (a) Comparison of stress computed using FEM and DEM along path 6 (see Figure 2b) ; (b) Histogram with the error (difference between the FEM and DEM results) for resulting after checking 485 positions located along the 9 paths indicated in Figure 2.

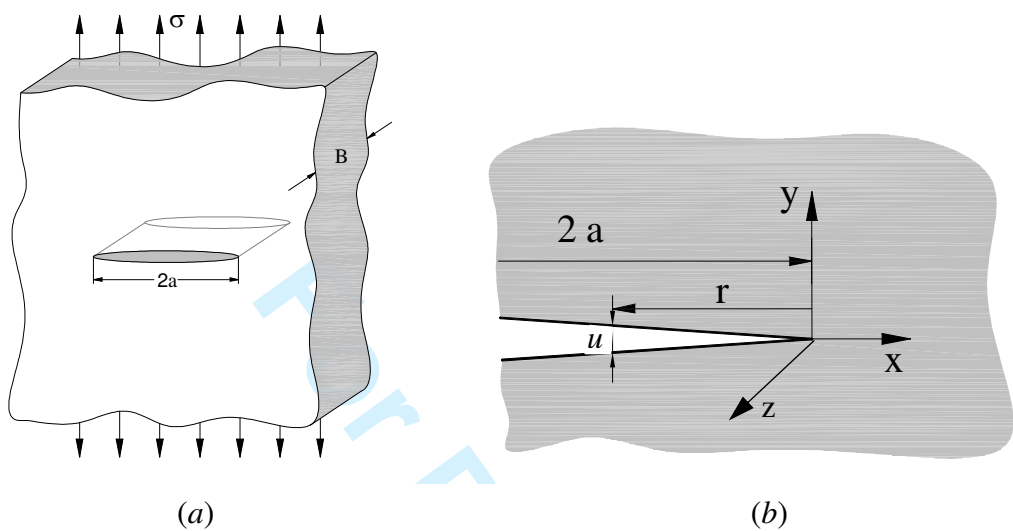


**Figure 4:** (a) A crack of length  $2a$  in a remotely load plate; (b) Relative displacement of the crack surfaces and local coordinate system at the crack tip.

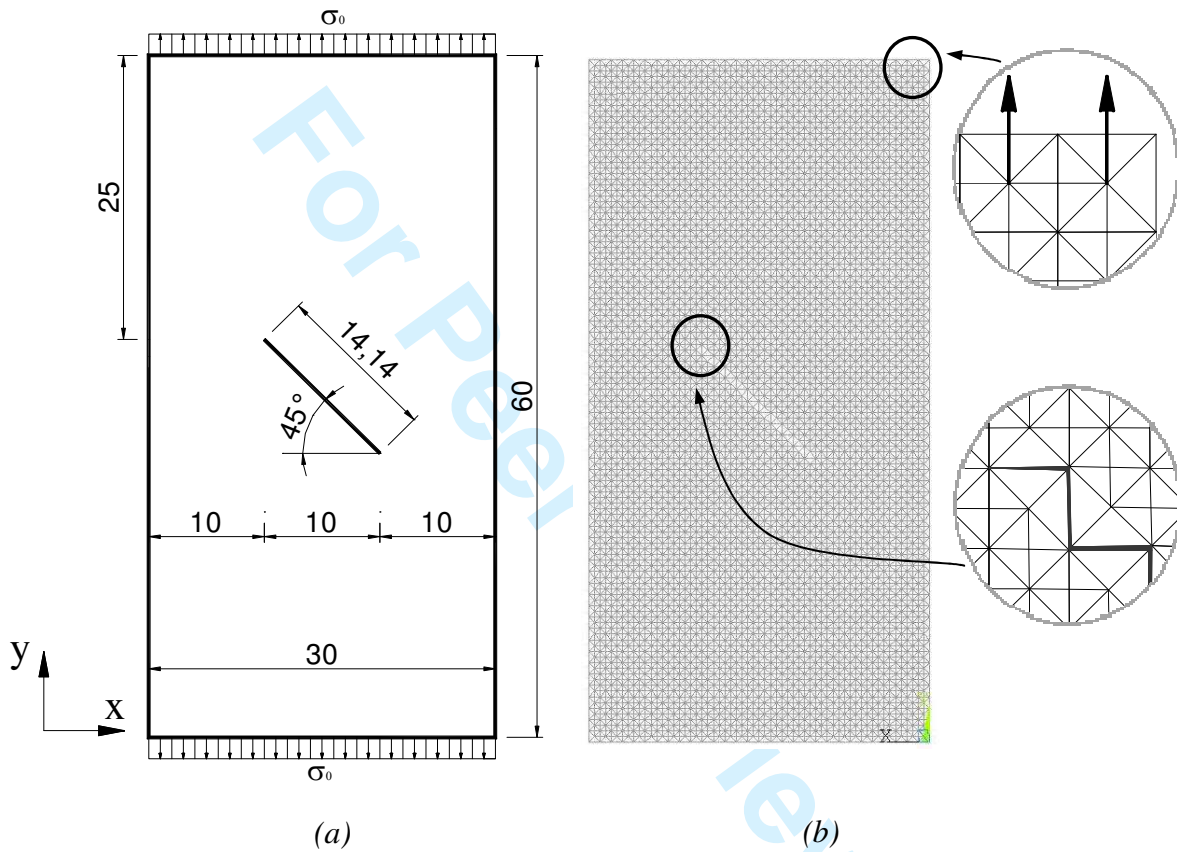


**Figure 5:** (a) Geometry and dimensions of the problem of the slant crack in a rectangular plate under impact loading (dimensions in mm); (b) Details of the DEM model.

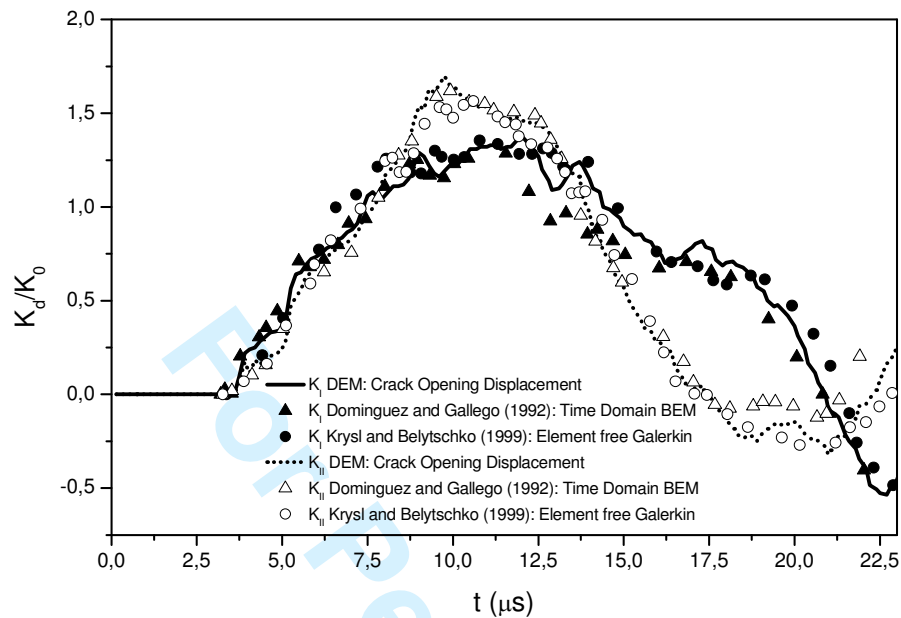


**Figure 6:** Time evolution of the mixed-mode dynamic stress intensity factors for the inclined crack in the rectangular plate.



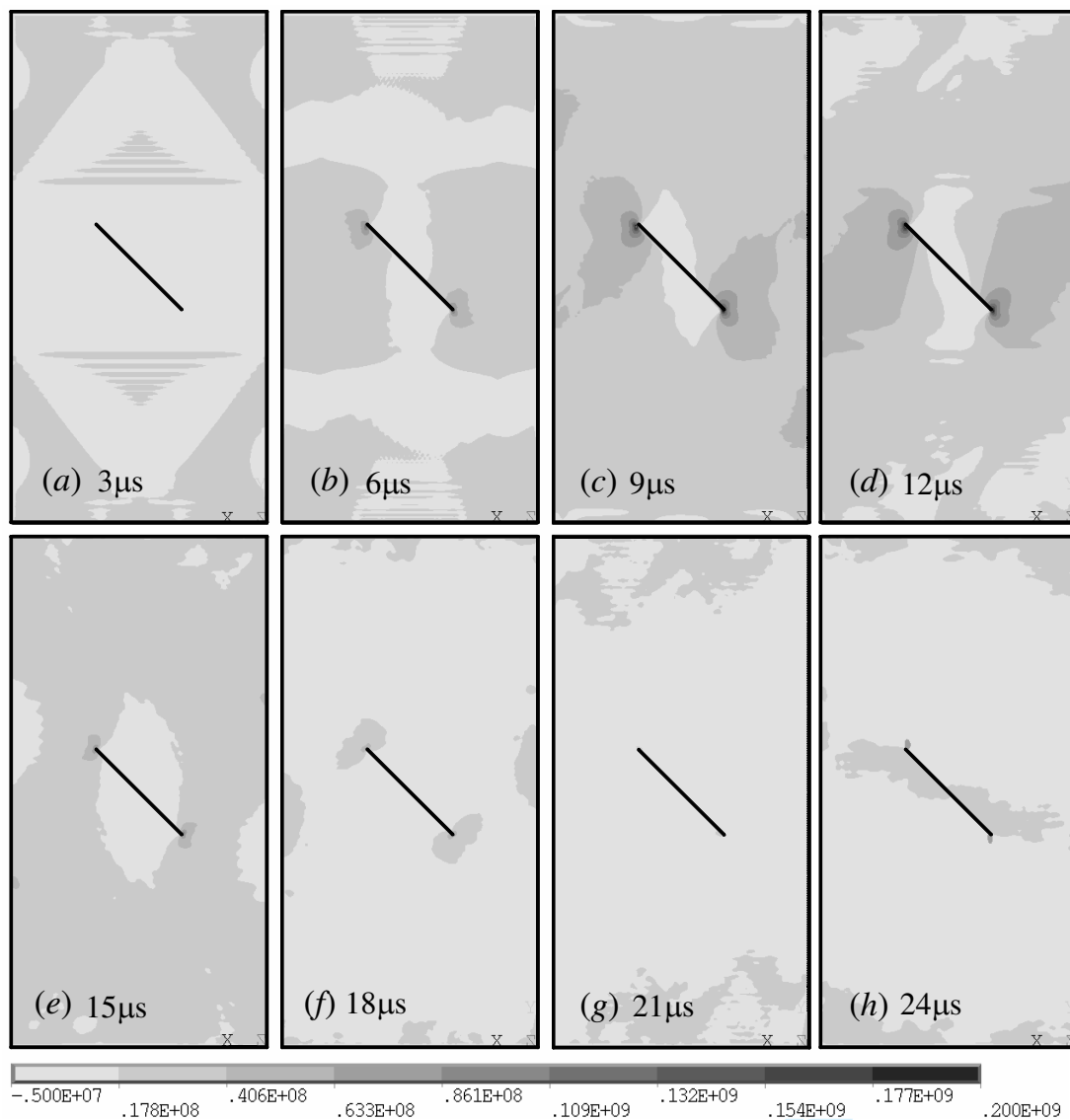


**Figure 7:** Time evolution of the of the maximum principal stress field for the example of the inclined crack in the rectangular plate.

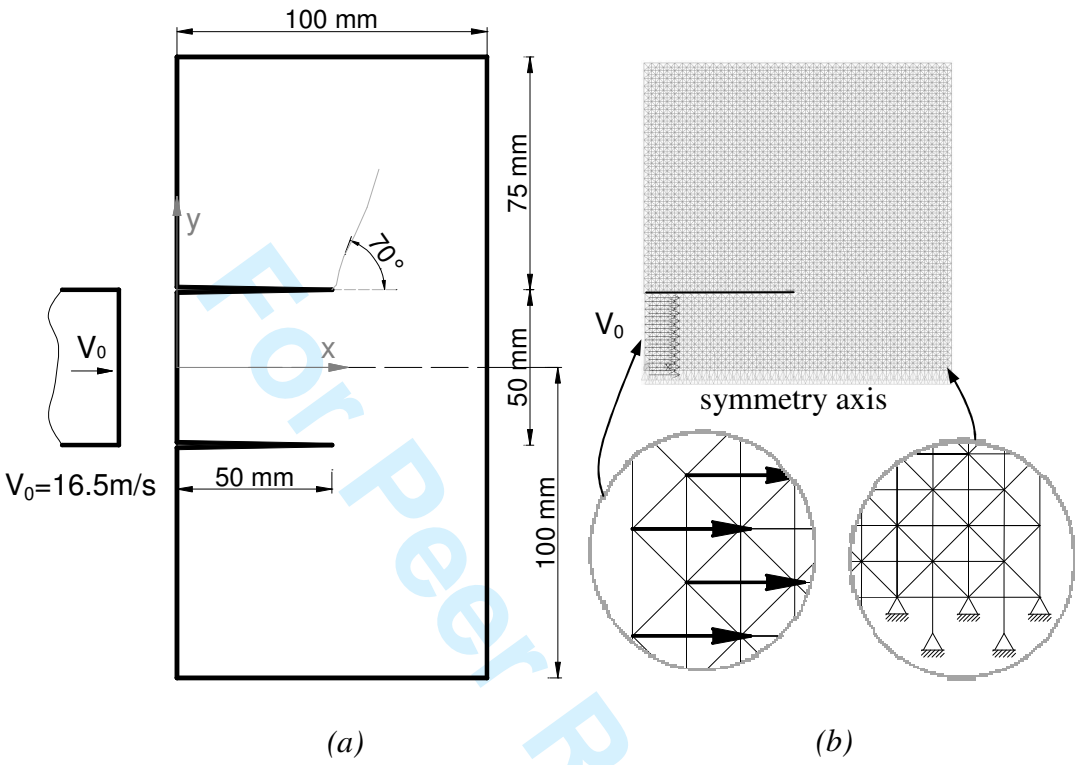


**Figure 8:** (a) Schematic of the Kalthoff-Winkler experiment; (b) DEM model details.

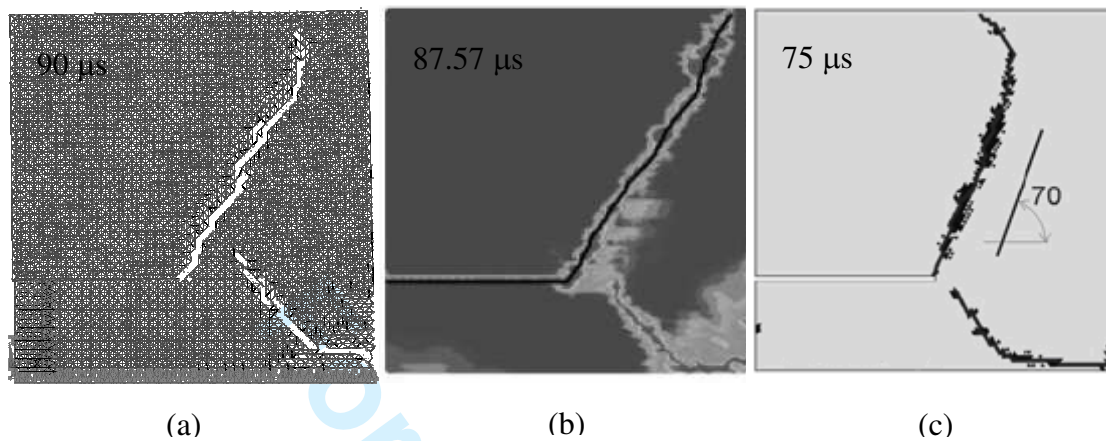


**Figure 9:** Fracture patterns for the Kalthoff-Winkler experiment: (a) DEM, this work; (b) XFEM from Belytschko et al. (2003); (c) Strong discontinuity approach with FEM from Huespe et al. (2006).

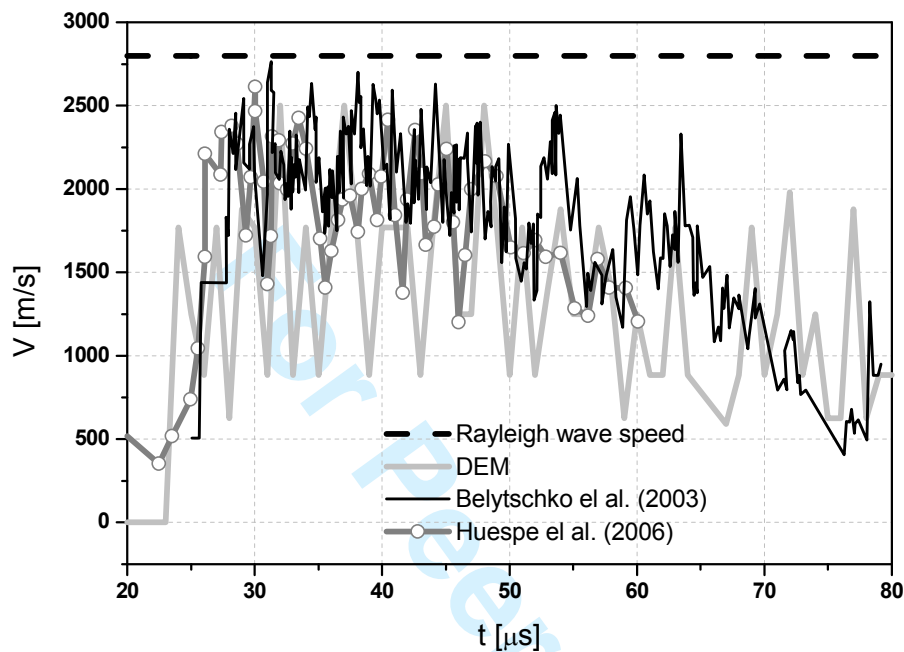


**Figure 10:** Crack propagation velocity as a function of time for the Kalthoff-Winkler experiment: (a) DEM, this work; (b) XFEM from Belytschko et al. (2003); (c) Strong discontinuity approach with FEM from Huespe et al. (2006).

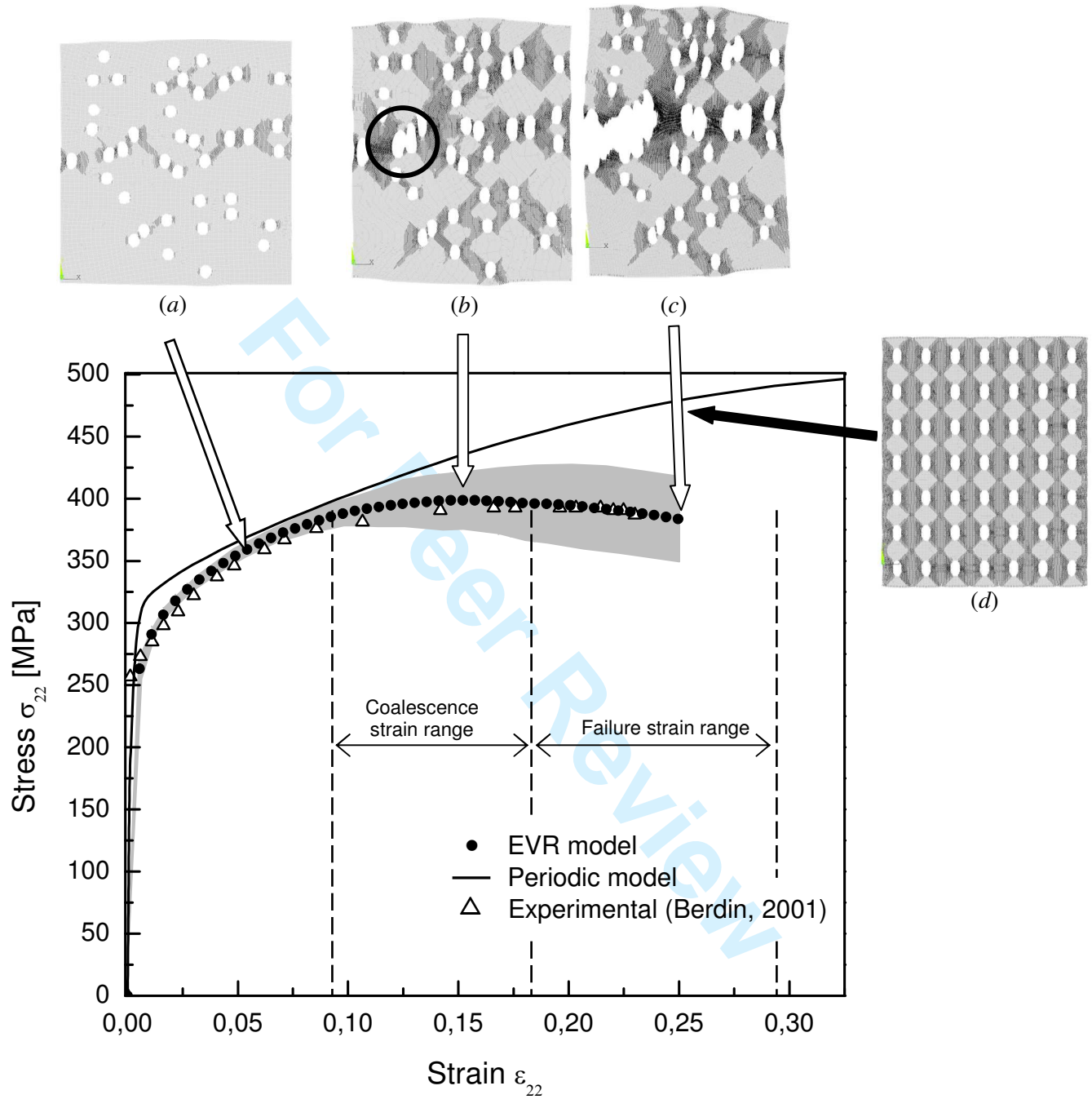


**Figure 11:** Uniaxial stress vs. strain curves for RVE and periodic models. Shaded area indicates the standard deviation of the RVE results.

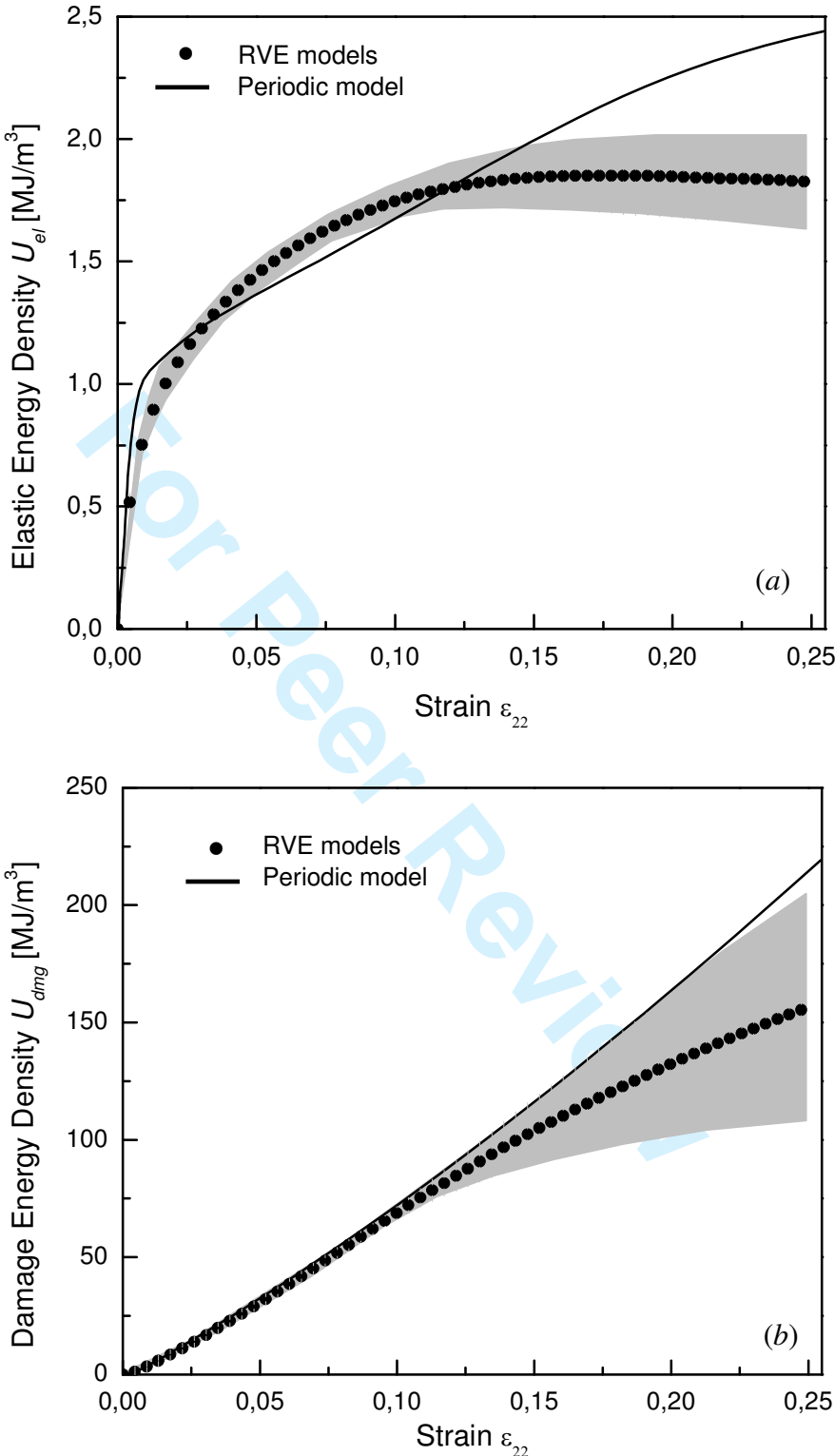


**Figure 12:** Evolution of the (a) elastic strain energy and (b) damage energy densities as functions of the longitudinal strain. Shaded areas indicate the standard deviation of the RVE results.